RSC Advances

PAPER

View Article Online
View Journal | View Issue

Cite this: *RSC Adv.*, 2025, **15**, 34861

Robust and self-healable polybenzimidazole membranes *via* Diels–Alder chain extension

Minjun Yin [ab] and Hongting Pu *[ab]

Despite the critical role of polybenzimidazole (PBI) in high-temperature membranes in fuel cells, its practical deployment remains hindered by inherent limitations including low molecular weight (<20 kDa), poor solution processability, and irreversible network formation upon conventional synthesis. To address these challenges, a dynamic covalent strategy was introduced, leveraging Diels–Alder (DA) chemistry for topological reconfiguration. By subjecting furan-functionalized PBI prepolymer (PBI-furan, M_n = 8.2 kDa) to bismaleimide chain extension, we achieve a fourfold increase in molecular weight (M_n = 32 kDa), yielding a reversibly crosslinked PBI-DA membrane. Compared to traditional PBI with the same molecular weight, this architecture synergistically integrates exceptional thermal stability (>450 °C onset decomposition), robust mechanical strength (tensile strength >80 MPa), suppressed phosphoric acid swelling (<10%) and elevated ionic conductivity. Crucially, the dynamic network enables cyclic reprocessability and autonomous self-healing, retaining >90% of the initial mechanical properties after three tensile cycles. Compared to static PBI networks, this system reduces irreversible chain entanglement, while maintaining performance parity. By deeply integrating dynamic covalent chemistry with PBI materials, this work not only advances the performance of high-temperature proton-exchange membranes but also establishes a novel framework for the sustainable design of green energy devices, presenting significant scientific merit and engineering application potential.

Received 9th August 2025
Accepted 15th September 2025

DOI: 10.1039/d5ra05834a

rsc.li/rsc-advances

1 Introduction

Polybenzimidazoles (PBIs) represent a class of aromatic heterocyclic polymers, with the first aliphatic chain-containing PBI synthesized by Keith in 1959 *via* the reaction of diacid and tetramin.[1] Besides, in heat-resistant fibers,[2] gas separation membranes,[3,4] organic solvent nanofiltration membranes[5] and aerospace technology,[6] the imidazole ring in PBI allows for both protonic acid and alkali doping, facilitating applications in high-temperature fuel cell membranes,[7–10] and sensors.[11] Recently, its application has been further extended to lithium-ion battery separators[12] and wear-resistant materials.[13]

PBI presents challenges in practical applications. Its high rigidity and strong intermolecular interaction contribute to excellent strength and stability.[14,15] However, excessively high molecular weight can lead to reduced solubility and flexibility, complicating membrane formation.[16] Therefore, the high molecular weight of PBI without reduced processibility is crucial for viable membrane production. To improve these defects, researchers have proposed various modification strategies to modify linear PBI, including copolymerization,[17–19] cross-linking,[20–22] the introduction of functionalized side chains, *etc.*[23] For example, ether bonds and hexafluoro isopropyl groups were incorporated to increase free volume and reduce hydrogen bonding among imidazole groups, thereby improving solubility.[24] However, this increased free volume may weaken the mechanical strength of PBI membranes. Zhu *et al.* prepared PBI with flexible alkyl sulfonic acid side chains, which showed a proton conductivity of 0.358 S cm^{-1} at 200 °C, but the thermal stability decreased by 7.8%.[25] Although covalent cross-linking can improve mechanical properties, it makes the material difficult to recycle due to irreversible cross-linking.[26,27] Therefore, the development of a PBI-based material with high stability, processability, and reversibility has become an important research direction in this field.

Dynamic Covalent Chemistry (DCC) constructs a material system through reversible covalent bonds, endowing materials with self-healing, re-moldable, and recyclable properties. The Diels–Alder reaction, as a classic dynamic covalent reaction, reversibly forms a six-membered ring structure between furan and maleimide under mild conditions.[28–31] Its bond energy is moderate, allowing it to dissociate at high temperatures and recombine at low temperatures. Inspired by this, we introduced the DA reaction into the molecular design of PBI to achieve advantages such as molecular weight regulation, improved processing performance, and green sustainability.

[a]*Key Laboratory of Advanced Civil Engineering Materials (Ministry of Education), School of Materials Science & Engineering, Tongji University, Shanghai, 201804, China. E-mail: puhongting@tongji.edu.cn*

[b]*Department of Polymer Materials, School of Materials Science & Engineering, Tongji University, Shanghai, 201804, China*

This study not only provides new ideas for the modification of PBI materials but also opens up a direction for the application of dynamic covalent chemistry in high-temperature proton exchange membranes. The PBI-DA membrane prepared by the DA chain extension strategy exhibits excellent proton conductivity and dimensional stability at high temperatures. At the same time, its reversible cross-linking property enables waste membranes to be recycled through simple heat treatment, which provides a potential way to reduce the full lifecycle cost of fuel cell systems. In addition, this material also shows potential in anion exchange membrane fuel cells, further expanding its application scenarios.

2 Experimental section

2.1 Materials

3,3′-Diaminobenzidine (DAB), isophthalic acid (IPA), *N*-methylpyrrolidine (NMP), polyphosphoric acid (PA), furoic acid, and ammonia water were purchased from Shanghai Aladdin Chemical Co. d_6-DMSO used as nuclear magnetic solvent was purchased from J&K Scientific. Ferrous sulfate heptahydrate, *N*,*N*′-(4,4′-methylenediphenyl)bismaleimide and ethanol were obtained from Energy Chemical Reagent Co. Hydrogen peroxide and KBr (the material for infrared tablet pressing) were bought from Sinopharm Chemical Reagent Co. All of the above reagents were used directly without further purification.

2.2 Preparation of the samples

2.2.1 Synthesis of oligomers (*m*-PBI-Am). A clean 150 mL three-necked flask was utilized to contain 150 g of polyphosphoric acid, which was stirred vigorously at 150 °C (rpm > 100 rpm) and subjected to vacuum drying for 30 min. Upon reaching 180 °C, vacuuming was ceased, and nitrogen gas was introduced into the system. Once the system was purged with nitrogen gas, 3,3′-diaminobenzidine (3.00 g, 14 mmol) was added, ensuring complete dissolution. After cooling to 150 °C, isophthalic acid (1.99 g, 12 mmol) was then incorporated. Following the full dispersion of the drug in the solvent, the mixture was heated to 195 °C and react for 6 h. The polyphosphate solution containing oligomers with specific viscosity was then slowly introduced into deionized water to terminate the reaction. The resultant product was soaked in ammonia water and stirred for 48 h to eliminate excess polyphosphoric acid from the polymer. Subsequently, the product was washed with deionized water until neutral and extracted for 24 h using a Soxhlet apparatus to remove impurities. The obtained oligomer was vacuum-dried at 120 °C for 24 h, yielding 3.809 g of reddish-brown powdery solid. The yield is 3.9%.

2.2.2 Synthesis of capped prepolymer (PBI-furan). 150 g of polyphosphoric acid was poured into a clean 150 mL three-necked flask, followed by rapid stirring at 120 °C and vacuum drying for 30 min. Subsequently, 0.025 g of furoic acid was added and allowed to dissolve completely. Then, 0.856 g of the previously obtained reddish-brown polymer (0.1 mmol, M_η = 8247.83) was introduced, and then the temperature was raised to 190 °C. The polymer solution transitioned from brownish-red to brownish-black as dissolution progressed. Once sufficient dissolution was achieved, the temperature was increased to 200 °C for 5 h to react. The reaction was terminated by slowly introducing a polymer solution of defined viscosity into deionized water, and the processing steps from Section 2.2.1 were repeated to obtain prepolymer products capped with furan, resulting in 0.731 g of black solid. The yield is 85.4%.

2.2.3 Synthesis of chain-extended polymer membrane (PBI-DA). A clean 100 mL three-necked flask was prepared with 50 mL of NMP solution and 0.731 g of PBI-furan, which was refluxed at 205 °C for 12 h under a nitrogen atmosphere to ensure complete dissolution of the product in NMP. After cooling the dissolved polymer solution to room temperature, it was transferred into a centrifuge tube and centrifuged at 10 000 rpm for 8 min to precipitate undissolved materials. The supernatant was filtered through a filter funnel to separate the precipitate, yielding the desired prepolymer solution with a concentration of 0.0206 g mL^{-1}. Then a total of 20 mL (0.412 g, 0.048 mmol) of the polymer solution was combined with 0.017 g bismaleimide at a ratio of 1 : 1 and thoroughly stired for 30 min, then subsequently poured into a clean square glass mold measuring 5 cm × 5 cm. The solvent was evaporated at 80 °C to form a membrane. After cooling to room temperature, the membrane was gently peeled off and washed repeatedly with distilled water to eliminate residual solvents and impurities. The membrane was then vacuum-dried at 105 °C until a constant weight was achieved, resulting in a chain-extended PBI polymer membrane. The dry membrane exhibited a smooth brown appearance with a thickness ranging from 15–25 μm.

2.2.4 Synthesis of control group (traditional *m*-PBI with corresponding molecular weight). The molar ratio of diaminobenzidine to isophthalic acid was adjusted to 1 : 1.1, and the final reaction was conducted at 210 °C for 12 h to prepare the brownish-black precipitate *m*-PBI according to the procedures outlined in Section 2.2.1.

2.3 Characterization of the samples

2.3.1 Structure and characterization of the samples. The characterization was conducted by using an AVANCE III HD 400 MHz liquid nuclear magnetic resonance spectrometer (Bruker BioSpin International, Switzerland) for the determination of ^{1}H NMR, operating at a frequency of 400 MHz with deuterated dimethyl sulfoxide (d_6-DMSO) as the solvent. The chemical composition and structure of both the prepolymer and chain-extended polymer were analyzed utilizing a Thermo Scientific Nicolet IS_5 Fourier transform infrared spectrometer (USA) in attenuated total reflection (ATR) mode, covering a scanning wavenumber range from 4000–400 cm^{-1} with a total of 32 scans.

2.3.2 Morphological characterization of the samples. The surface and cross-sectional morphology (liquid nitrogen embrittlement) of each group of samples were observed using the field emission scanning electron microscope (Gemini SEM 500 instrument SEM, equipped with X-ray energy spectrometer, Zeiss company). EDS surface scanning was used to collect X-rays to calculate the relative content of elements and form an element distribution map.

2.3.3 Molecular weight determination. The intrinsic viscosity η was measured using an Ubbelohde viscometer maintained at a constant temperature of 30 °C ± 0.1 °C, employing 20 mL 96% concentrated sulfuric acid as the solvent for preparing five different concentrations of polymer solutions (0.2 g dL^{-1}, 0.4 g dL^{-1}, 0.6 g dL^{-1}, 0.8 g dL^{-1} and 1.0 g dL^{-1}). The viscosity-average molecular weight of the polymer was calculated according to the Mark–Houwink–Sakurada equation: $\eta_{int} = 1.94 \times 10^{-4} M_{\eta}^{0.791}$.

2.3.4 Mechanical properties. Mechanical properties were evaluated following national standard GB/T1040.4-2006 using a UTM2502 mechanical tester (Suns Technology Co.). All samples were cut into standard type IV dumbbell-shaped specimens; testing occurred at room temperature under identical tensile conditions. The tensile rate was 5 mm min^{-1} at room temperature. Each type of polymer film was tested at least three times to ensure the accuracy of the test.

2.3.5 Solubility. Clean culture bottles with a volume of 10 mL were prepared, into which 0.050 g of polymer was added to 3 mL of NMP. The mixture was stirred at varying temperatures (70 °C and 130 °C) for a duration of 24 h. If the polymer was not completely dissolved, additional NMP was added for further stirrin. 1 mL of solution were weighed using a pipette, when the mass variation was less than 0.001 g between consecutive measurements, recorded the mass of the dissolved solution as m_2, where m_1 is the mass of the sample before dissolution extraction. The amount X of soluble polymer was calculated using eqn (1).

$$X = \frac{m_2}{m_1} \times 100\% \quad (1)$$

2.3.6 Thermal stability. Thermal gravimetric analysis (TGA) of the polymer was conducted using a NETZSCH STA449C thermal analyzer. Before the test, all the membranes were dried at 105 °C for 24 h to remove residual water on the surface of the dry film. The test conditions were a nitrogen atmosphere and a heating rate of 10 °C min^{-1} from 30 °C to 1000 °C.

2.3.7 Oxidation stability. The polymer membrane was dried in a vacuum oven at 100 °C until a constant weight was achieved, and then quickly weighed on an analytical balance, with the initial mass recorded. The membrane was then placed in Fenton's reagent (4 ppm Fe^{2+}, 3% H_2O_2), where Fe^{2+} was obtained by dissolving $FeSO_4 \cdot 7H_2O$ in deionized water. The mixture was maintained at 70 °C for 24 h, after which the membrane was removed and dried in a vacuum oven at 100 °C until a constant weight was reached. It was then quickly weighed again on an analytical balance. A fresh batch of Fenton's reagent was prepared, and the process was repeated seven times. The antioxidant property of the membrane was determined based on the change in mass.

2.3.8 Dimensional stability. The membrane was cut into 10 mm × 10 mm rectangular specimens, dried in a 100 °C vacuum oven until constant weight, and then the weight m_0, length a_0, width b_0, and thickness c_0 of the membrane were measured. The membranes were respectively immersed in distilled water at 80 °C for different durations (6 h, 18 h, 24 h, 48 h, 72 h, 96 h, 120 h, 144 h). After removal, the excess water on the surface was quickly wiped dry with a moist filter paper. The wet weight (m_i), length (a_i), width (b_i), and thickness (c_i) of the membranes were remeasured and recorded. The water uptake (WU) and swelling ratio (SR) of the membranes were calculated according to Formulas (2) and (3) respectively.

$$WU = \frac{m_{wet} - m_{dry}}{m_{dry}} \times 100\% \quad (2)$$

$$SR = \frac{a_i b_i c_i - a_0 b_0 c_0}{a_i b_i c_i} \times 100\% \quad (3)$$

2.3.9 Water contact angle test. The contact angles were performed by measuring the contact angle between the membranes and water, or between the membranes and phosphoric acid at room temperature using JYC-2 (Fangrui, Shanghai).

2.3.10 ADL and swelling test in phosphoric acid. The membranes were dried at 105 °C for a period of 24 h to determine their dry weight M_{dry} and length L_{dry}. Following this process, they were immersed in an aqueous solution containing 85 wt% H_3PO_4 at room temperature. The weights M and lengths L were recorded after intervals of 6 h, 18 h, 24 h, 48 h, and 72 h. From these measurements, the phosphoric acid doping level (ADL) and swelling ratio (SW) of the membrane in phosphoric acid were calculated using eqn (4) and (5).

$$ADL = \frac{(M - M_{dry})/M_{PA}}{M_{dry}/M_{PBI}} \times 100\% \quad (4)$$

$$SW = \frac{L - L_{dry}}{L_{dry}} \times 100\% \quad (5)$$

2.3.11 Conductivity. The proton conductivity (σ) of the membrane was calculated by measuring the impedance with four probes on an electrochemical impedance spectrometer CHI 660C (CH Instruments), the schematic diagram is as follows. The pre-dried membrane was sandwiched between two circular copper electrodes (d = 0.75 cm) and fixed in a high-pressure autoclave. The autoclave was heated in a sand bath, and the conductivity of the membrane was measured at different temperatures. The σ (S cm^{-1}) was calculated using Formula (6), where R (Ω) represents the ohmic resistance measured by the impedance spectrometer. Both L (cm) and A (cm^2) were measured with a vernier caliper. L (cm) refers to the distance between the two current-carrying electrodes, which is the thickness of the membrane. A (cm^2) is the effective contact area between the membrane and the electrode, which is the area of the circular copper electrode. To ensure quantitative comparison of the results, three samples were taken from each proportion for measurement, and the average value was calculated.

$$\sigma = \frac{L}{ZA} \quad (6)$$

2.3.12 Self-healing and recycling performance. The polymer membrane doped with phosphoric acid was divided into two parts, and then place the fracture surface in close contact on

a hot stage at 120 °C. After cooling to room temperature, observe the fracture surface to evaluate whether the membrane has self-healing properties. To investigate the reversible characteristics of the membranes, repeated mechanical performance tests were subjected. Strips of PBI-DA membranes were immersed in a polyphosphoric acid solution at room temperature for 12 h, followed by drying for the initial mechanical property test. Afterwards, divide the strip into two parts and cut off a corner at the top as a marker. Place the fracture surface in close contact on a hot stage set to 120 °C for 45 min, after returning to room temperature, the membrane solidified again and was held at room temperature for 24 h prior to a second mechanical property assessment. This procedure was repeated to generate the cyclic tensile curves for PBI-DA. The tensile strength and elongation at break of the original sample are recorded as σ_0 and ε_0, the tensile strength and elongation at break of the repaired samples are recorded as σ_i and ε_i. Healing efficiency of strength η_1 and elongation η_2 were calculated using eqn (7) and (8).

$$\eta_1 = \frac{\sigma_i}{\sigma_0} \times 100\% \quad (7)$$

$$\eta_2 = \frac{\varepsilon_i}{\varepsilon_0} \times 100\% \quad (8)$$

3 Results and discussion

3.1 Preparation of the samples

The synthetic strategy employed in this study is illustrated in Scheme 1: *m*-PBI-Am was synthesized through melt polymerization utilizing polyphosphoric acid as the solvent,[32] while low molecular weight prepolymer PBI-furan was produced *via* furan capping. Low molecular weight linear prepolymers were dissolved in NMP solvent, followed by the addition of bismaleimide, leading to the formation of long-chain polymers *via* the DA reaction.[33–35]

Concurrently, meta phenyl *m*-PBI, which have a molecular weight comparable to that of the extended chain polymer, was synthesized to investigate the effects of DA bond formation on the properties of PBI. Meanwhile, Table 1 lists the η, M_η of different polymers (Fig. S1–S4 in (SI)).

3.2 Structure and characterization of the samples

Fig. 1a shows the ^{1}H NMR spectra of PBI-furan and PBI-DA. The peak at $\delta = 13.27$ ppm is attributed to the –NH– group on the imidazole ring, while the peaks *b*–*f* ($\delta = 7$–9 ppm) correspond to hydrogen atoms on the benzene ring. Peaks *g*–*l* represent the protons on the 2-substituted furan. The double peaks at *j* ($\delta =$ 5.32 ppm), the proton peaks at *k*, *m*, and *n* correspond to the protons in the DA addition product.[36,37] The nuclear magnetic resonance spectrum confirms the successful synthesis of PBI-furan and PBI-DA.

In addition, the infrared spectrum (Fig. 1b) provides information on the corresponding functional groups. An –N–H– stretching vibration peak indicative of PBI was detected within the range of 2500–4000 cm^{-1}. Peaks observed at 1533.82 cm^{-1}, 1066.01 cm^{-1}, and 846.41 cm^{-1} are associated with the C=C, C–O–C, and C–H bonds of furan,[37] respectively. Additionally, the double peaks of *m*-PBI Am between 3064–2799 cm^{-1}

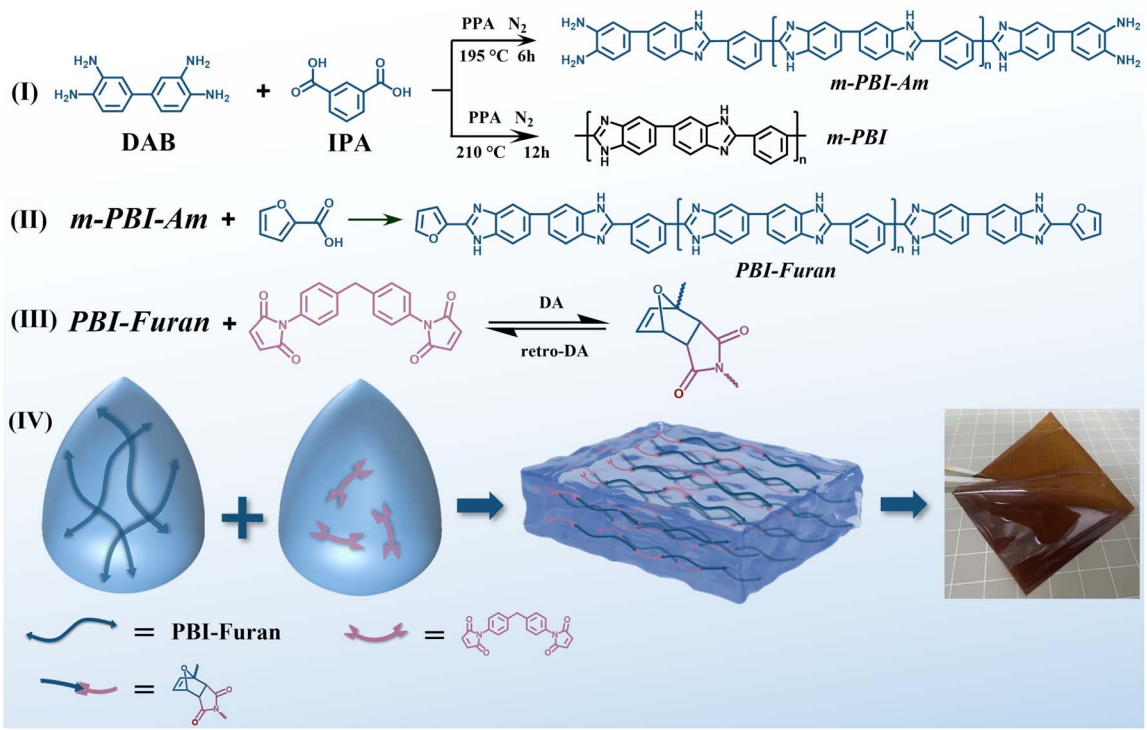

Scheme 1 Synthesis route of the polymers: (I) low molecular weight *m*-PBI Am and *m*-PBI as the control group. (II) Furan-capped prepolymer (PBI-furan). (III) Chain extended polymer (PBI-DA). (IV) Solution pouring and preparation for film formation.

Table 1 η, M_η of *m*-PBI-Am, PBI-DA and *m*-PBI

Samples	η (dL g^{-1})	M_η (g mol^{-1})
m-PBI-Am/PBI-furan	24.3	8248.83
PBI-DA	72.73	32 974.69
m-PBI	76.71	35 273.48
PBI-DA (170 °C)	40.85	15 903.93

diminished to the point of disappearance, indicating that the amino group at the terminal end of PBI underwent reaction, confirming the successful capping of furan at both ends of *m*-PBI-Am. Following the DA reaction, C=O and C–N–C peaks in the bismaleimide ring were observed at 1885.62 cm^{-1} and 1393.46 cm^{-1}, respectively, and a more pronounced stretching vibration of C=C was noted, suggesting the effective completion of the DA reaction.

Based on the information provided by infrared spectroscopy analysis and nuclear magnetic resonance spectroscopy, both the prepolymer and long-chain polymer were successfully synthesized.

3.3 Morphological characterization of the samples

The material was prepared into membranes by solution casting method,[38] then the material structure was characterized by SEM (Fig. 2a–2c1) and EDS (Fig. 2a2–2c2), the thickness of the tested membrane was 20 μm, all the samples were fractured in liquid nitrogen and treated with Pt coating before testing to enhance their conductivity. As shown in the cross-sectional SEM images of Fig. 2a–c, before chain extension, PBI-furan forms a layered structure during the solution casting process (Fig. 2a). After chain extension, as the molecular weight increases, higher molecular chain entanglement and stacking make the material structure more compact, forming a denser membrane structure, as shown in the PBI-DA cross-section (Fig. 2b). *m*-PBI with the same molecular weight also exhibits similar cross-sectional morphology (Fig. 2c). Similarly, from the surface morphology of the sample, it can be observed that the surface of the membrane formed by the prepolymer PBI-furan is uneven (Fig. 2a1), while the higher molecular weight PBI-DA and *m*-PBI form a denser and more uniform membrane surface (Fig. 2b1–2c1). The element distribution map and content obtained from EDS (Fig. 2a2–2c2 and Table 2) can also show that the distribution of C element becomes denser with the increase of molecular weight, which corresponds to the trend in SEM images. The small amount of O element contained in *m*-PBI may come from the water absorbed by the PBI membrane.

3.4 Solubility test

The processing performance of PBI is influenced by its soluble content in organic solvents, with the soluble portion of different PBIs in NMP depicted in the subsequent Fig. 3. An increase in temperature results in a significant enhancement in the solubility of all three types. This phenomenon is attributed to the accelerated movement of solute molecules and the increased distance between liquid molecules at elevated temperatures, facilitating solute dissolution. Furthermore, at 70 °C, PBI-furan exhibited the highest solubility due to its lower molecular weight. The solubility of chain-extended PBI-DA was found to be slightly greater than that of m-phenyl *m*-PBI. It is postulated that the presence of DA bonds disrupts the regular arrangement of –NH– bonds, diminishes intermolecular hydrogen bonding interactions, and reduces the rigidity of certain PBI structures. At 130 °C, the solubility of PBI-DA markedly increased, attributed to the cleavage of DA bonds at high temperatures, leading to the degradation of long-chain polymers into smaller

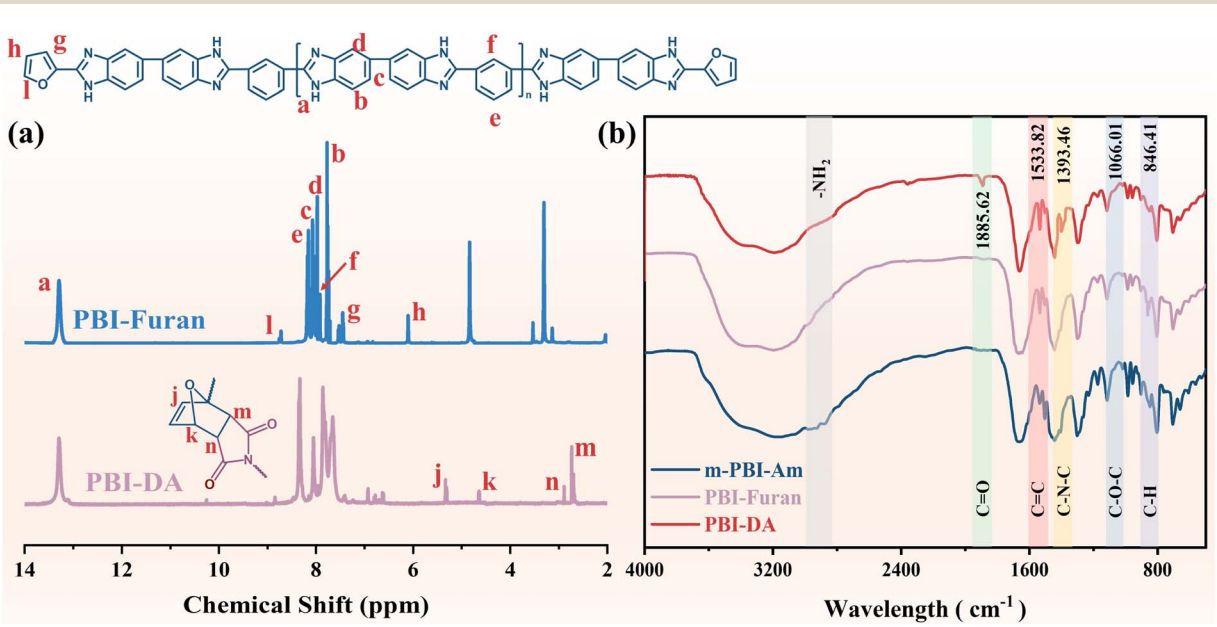

Fig. 1 (a) ^{1}H NMR spectra of prepolymer PBI-furan and chain-extended polymer PBI-DA. (b) FT-IR spectra of prepolymer PBI-furan, chain-extended polymer PBI-DA and *m*-PBI-Am.

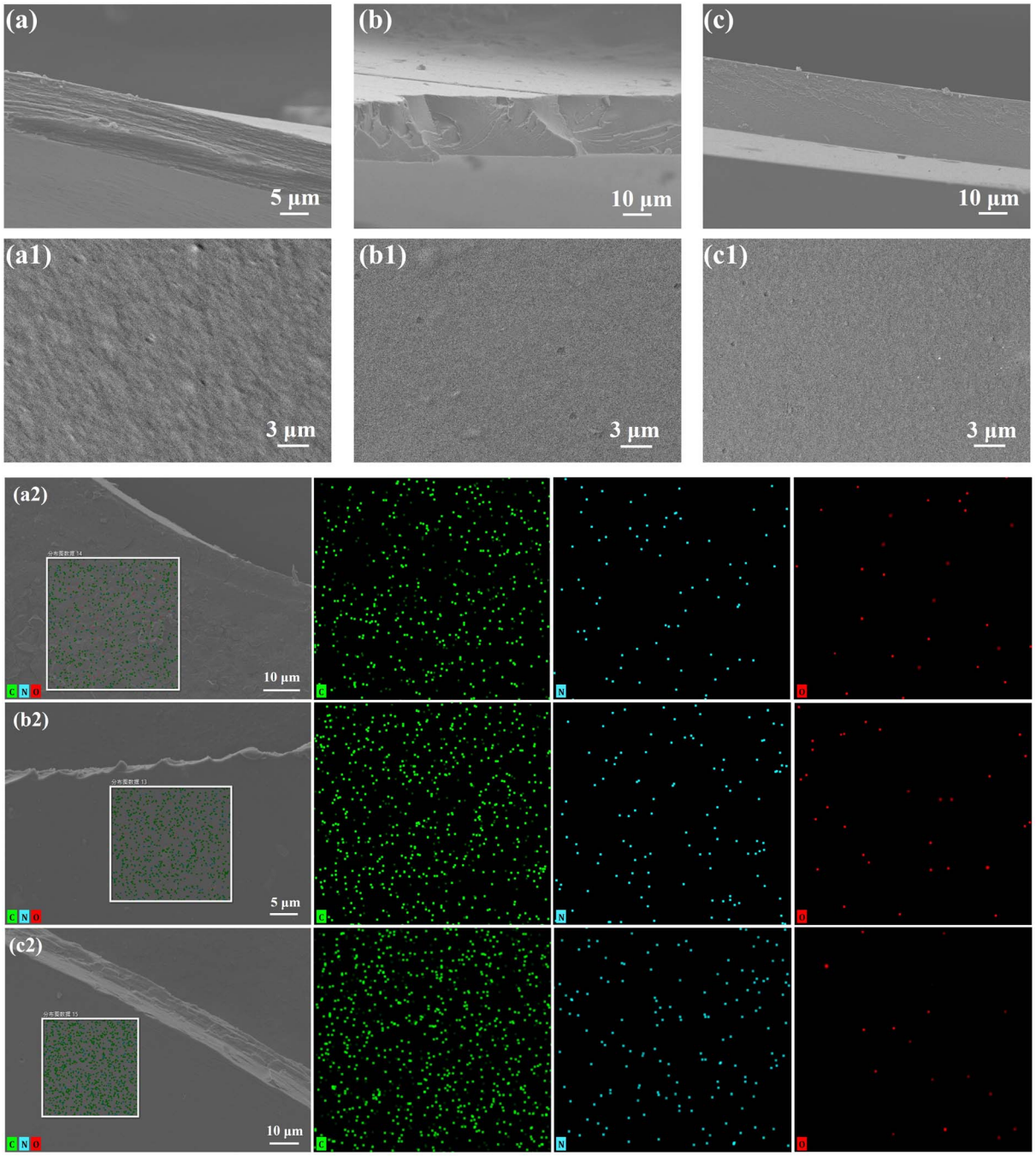

Fig. 2 The cross-sectional SEM images of (a) PBI-furan, (b) PBI-DA and (c) *m*-PBI (treated with Pt coating after fractured in liquid nitrogen). The surface SEM image of (a1) PBI-furan, (b1) PBI-DA and (c1) *m*-PBI (treated with Pt coating after fractured in liquid nitrogen). The distribution of C, N, O element from EDS maps of (a2) PBI-furan, (b2) PBI-DA and (c2) *m*-PBI.

Table 2 The distribution and content of different samples

Samples	C (wt%)	N (wt%)	O (wt%)
PBI-furan	78.94	15.72	5.34
PBI-DA	82.08	13.39	4.62
m-PBI	83.76	15.41	0.83

prepolymer molecules, thereby enhancing their dissolution in solvents.

3.5 Phosphate doping kinetics and swelling kinetics of the samples

As a crucial anhydrous proton exchange membrane, PBI requires acid doping to develop proton transfer capabilities

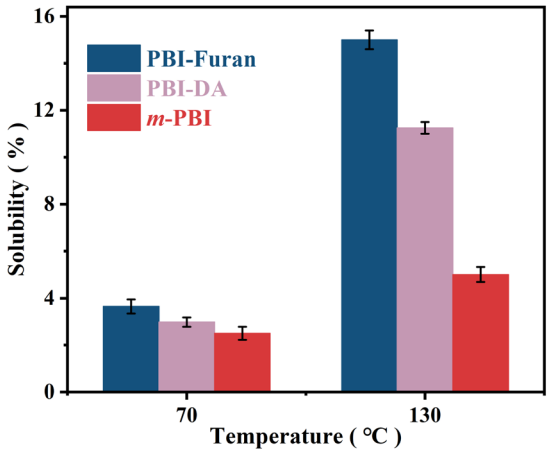

Fig. 3 The solubility of PBI-furan, PBI-DA and *m*-PBI in NMP at different temperatures.

through the dissociation of acid molecules.[39] Therefore, investigating the kinetics of phosphate doping in PBI membranes is essential for their application in fuel cells. We assessed the phosphate doping level in PBI membranes and investigated the swelling kinetics of the membranes in phosphate after accounting for the influence of monomer mass (Fig. 4e and f). The results indicate that the ADL growth rate of the membrane is rapid during the first 12 h, followed by a decline, eventually stabilizing after 24 h. This behavior occurs because, upon immersion in an 85 wt% phosphoric acid solution, the membrane absorbs a significant amount of water due to hydrogen bonding between monomers, leading to a considerable weight increase. As the concentration gradient between the interior and exterior of the membrane rises, there is an exchange of phosphate molecules from the outside with water molecules from within the membrane until equilibrium is achieved. The swelling of the membrane in the phosphoric acid solution exhibited a similar pattern.

The specific characteristics of PBI associated with phosphate doping are primarily observed in two key aspects: phosphophilicity and phosphate absorption. The molecular weight of PBI is a critical factor influencing the kinetics of phosphate doping. It can be seen that PBI-furan exhibits a relatively loose membrane structure due to its low molecular weight (combined with Fig. 2a), facilitating the ingress of phosphoric acid molecules for doping. As the molecular chain extends and the density of the membrane increases, there is an enhancement in the uniformity and stability of phosphate doping, which enhances phosphophilicity, manifested as the decreased contact angle shown in the Fig. 4d. Conversely, with an ongoing increase in molecular weight, the denser molecular chains pose greater resistance to phosphate absorption, as evidenced by the reduced phosphate absorption rate of PBI-DA within 30 s and the accumulation of phosphoric acid on the surface of the *m*-PBI, as illustrated in Fig. 4d. At equivalent molecular weights, PBI-DA demonstrates a greater doping capacity compared to *m*-PBI, which may be due to the introduction of DA covalent bonds that create additional space between molecular chains, thereby permitting some phosphoric acid to penetrate.

3.6 Mechanical properties of the samples

The change in mechanical strength is also an important factor reflecting the structural changes of polymers. The mechanical properties of acid-doped and undoped membranes measured at

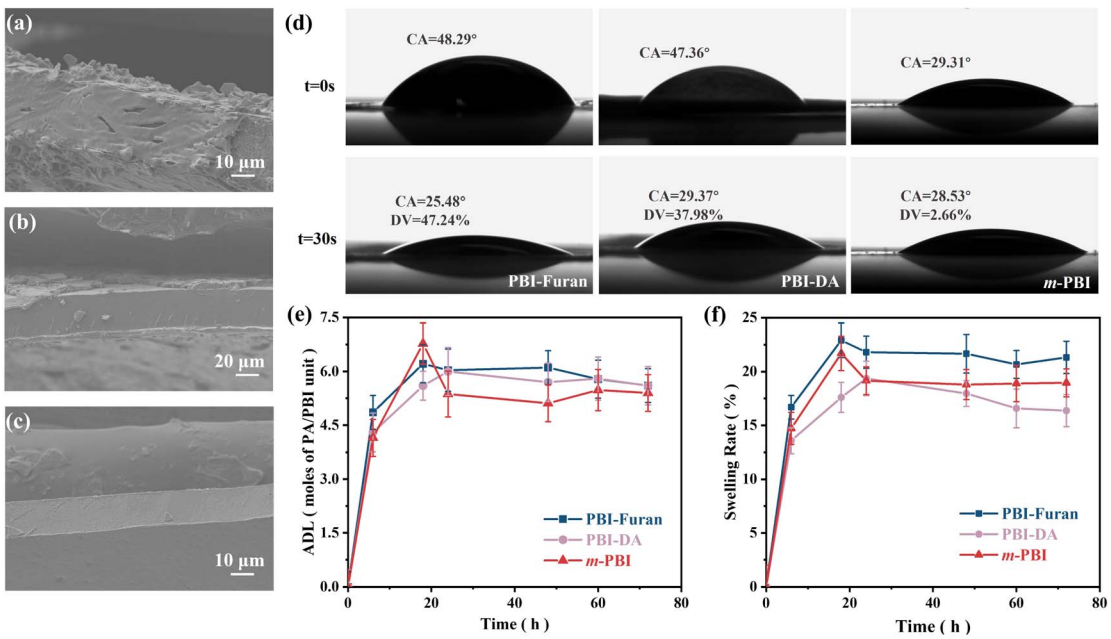

Fig. 4 The cross-sectional SEM images of (a) PBI-furan, (b) PBI-DA and (c) *m*-PBI all doped with phosphate acid (fractured in liquid nitrogen). (d) Phosphate acid contact angle of different polymer membranes at 0 s and 30 s. (e) ADL and (f) swelling ratio of PBI-furan, PBI-DA and *m*-PBI in phosphoric acid.

Table 3 Mechanical properties of phosphoric acid doped and undoped membranes. Test temperature: room temperature, stretching rate: 5 mm min^{-1}

Samples	PA doped	Tensile strength (MPa)	Elongation at break (%)	Young's modulus (GPa)	Toughness (MJ m^{-3})
PBI-furan (d = 18 μm)	No	47.48	4.58	1.47	1.13
	Yes (ADL = 5.3)	5.97	8.97	0.096	0.34
PBI-DA (d = 21 μm)	No	75.33	25.14	2.73	15.80
	Yes (ADL = 5.1)	19.71	62.81	0.13	8.41
m-PBI (d = 20 μm)	No	89.53	17.93	3.02	13.96
	Yes (ADL = 5.1)	21.62	24.36	0.15	2.96

room temperature are summarized in Table 3 (Fig. S5 and S6 in SI). Before chain extension, the stress of undoped PBI-furan was 47.48 MPa, with a fracture elongation of only 4.58%, indicating the low strength and brittleness of the material. After chain extension, the tensile strength and elongation at break of PBI-DA were significantly improved, reaching 75.33 MPa and 25.14%, respectively indicating the successful DA reaction. Meanwhile, compared to *m*-PBI with the same molecular weight, the tensile strength slightly decreased, but the elongation at break significantly increased, indicating that the introduction of DA covalent bonds significantly increased the toughness of the material. The stress–strain of the polymer membrane after acid doping also represented the same trend. The tensile strength of PBI-DA was comparable to *m*-PBI, while the elongation at break increased to 62.81%, which was seven times that of the PBI-furan and three times that of *m*-PBI. This further substantiates that the incorporation of DA bonds enhances the toughness of the material, albeit at the expense of some mechanical strength.

3.7 Stability of the membranes

PBI is capable of absorbing substantial amounts of water *via* hydrogen bonding, which impacts the dimensional stability of the membrane.[40] Given the operational conditions of high-

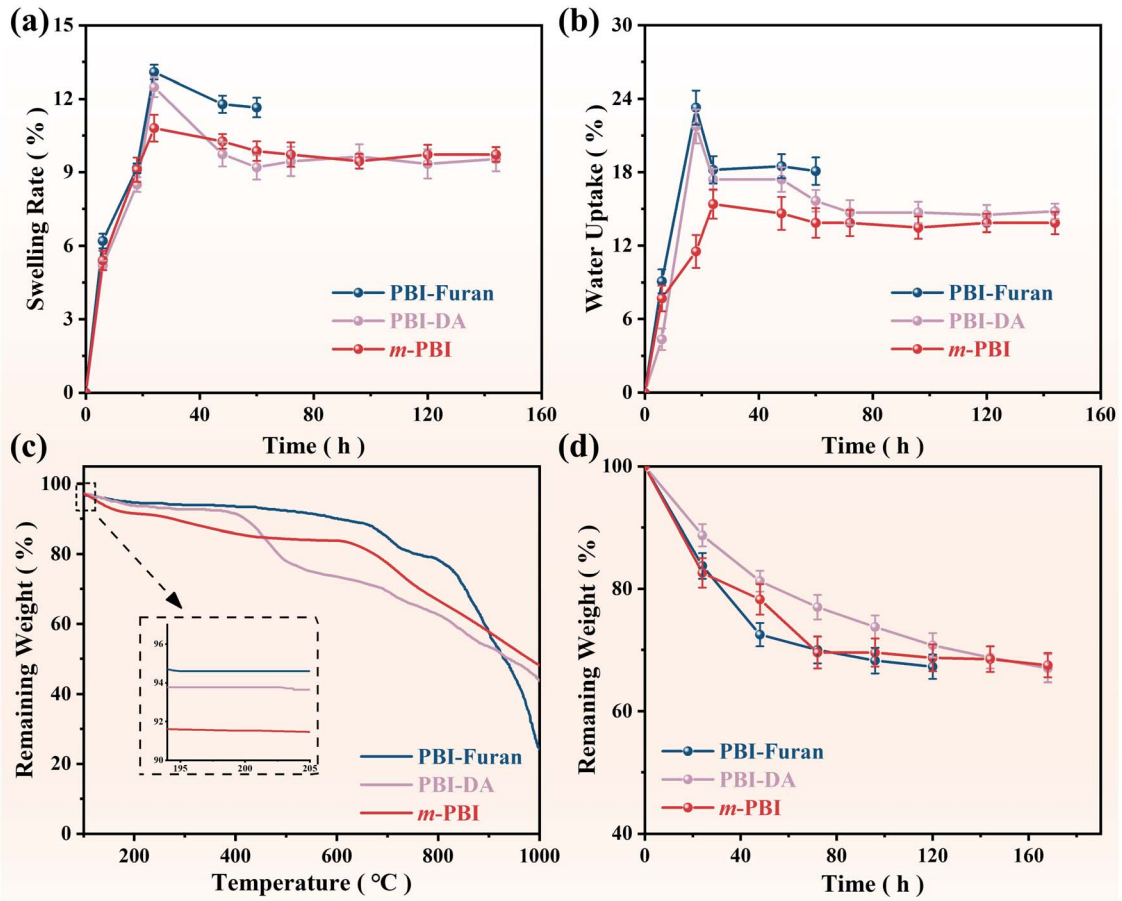

Fig. 5 (a) Water uptake and (b) swelling ratio at 80 °C of PBI-furan, PBI-DA and *m*-PBI. (c) The remaining weight from TG of PBI-furan, PBI-DA and *m*-PBI. Test conditions: room temperature ~1000 °C, nitrogen atmosphere, heating rate: 10 °C min^{-1}. (d) The antioxidant stability curves of PBI-furan, PBI-DA and *m*-PBI. Test conditions: Fenton reagent (4 ppm Fe^{2+}, 3% H_2O_2, incubated at 70 °C for 24 h).

temperature proton exchange membrane fuel cell (HT-PEMFC), the water absorption and swelling rates of the membrane were evaluated (Fig. 5a and b). The polymer membrane was subjected to testing at 80 °C, revealing a pronounced increase in water absorption and volumetrie swelling within the initial 36 h, seemingly linked to molecular weight. As molecular weight increased, both water absorption and swelling rates declined before stabilizing at 36 h. After 48 h, both parameters began to decrease gradually, indicating that the membrane achieved equilibrium in water absorption and swelling rate. It is noteworthy that the prepolymer's low molecular weight resulted in insufficient mechanical strength, leading to membrane failure at 60 h due to excessive water absorption. After 144 h, the water absorption rates of PBI-DA and *m*-PBI were observed to be closely comparable at 9.52% and 9.64%, respectively. Nevertheless, PBI-DA demonstrated higher volumetric expansion with reduced water absorption, suggesting a slight decrease in size stability of the chain-extended membrane.

The thermal stability and durability of polymer membranes are essential for ensuring their safety during application. Thermogravimetric analysis was performed on the samples by heating from 30 °C to 1000 °C in a nitrogen atmosphere (Fig. 5c). The thermal degradation of the membranes can be categorized into three distinct phases: (i) the initial weight loss observed prior to 200 °C is attributed to the evaporation of bound water and hydrogen-bonded water within the samples.[41,42] The respective weight losses at 200 °C for PBI-furan, PBI-DA, and *m*-PBI were recorded at 5.43%, 6.2%, and 8.5%. An increase in molecular weight correlates with enhanced hygroscopicity of the polymer membranes. (ii) Beyond 200 °C, the degradation of hydrogen bonds and the evaporation of residual solvent result in a decrease in membrane mass between 200 °C and 600 °C. Notably, PBI-DA experiences considerable mass loss between 400 °C and 500 °C due to bismaleimide decomposition. (iii) After 600 °C, a third weight loss phase is identifiable, associated with the degradation of the PBI backbone. Concurrently, furan ring decomposition initiates around 670 °C, leading to a more pronounced mass reduction in PBI furan compared to other polymer membranes, particularly noticeable at 667 °C. At 1000 °C, PBI-DA retains over 40% of its initial mass, significantly surpassing the prepolymer, thereby affirming the effective chain extension of the polymer.

The durability of a membrane largely depends on its antioxidant stability.[43–45] The membrane's durability primarily hinges on its antioxidant stability (Fig. 5d). The antioxidant capacity of the samples was assessed using a fractional reagent. In the presence of Fe^{2+} ions, H_2O_2 catalyzes decomposition, generating free radicals such as ·OH and ·OOH, which compromise the polymer matrix and result in membrane deterioration.[46] All samples were submerged in Fenton's reagent and maintained at 70 °C, then removed at every 24 h in to record remaining weight and failure time. As illustrated, the prepolymer fractured after 120 h, with the weight at failure being 66.8% of its original mass. Both PBI-DA and *m*-PBI demonstrated robust antioxidant stability, with weight losses of 32.58% and 33.11% after 168 h, respectively, while preserving the integrity of the membrane morphology. However, it should be noted that the mass of meta phenyl *m*-PBI remained largely unchanged after 72 h, whereas PBI-DA exhibited greater mass loss. We speculate that this may be related to the presence of dynamic covalent bonds in the material.

3.8 Conductivity of the membranes

Polybenzimidazole has been widely studied in the field of fuel cells due to its excellent thermal, mechanical, and chemical stability. We objectively assessed the viability of PBI membranes for use in proton exchange membrane fuel cells (PEMFCs) and anion exchange membrane fuel cells (AEMFCs), using four electrode AC impedance method (Fig. 6a and S7 in SI).

The proton conductivity of the membrane was evaluated at 0% relative humidity, maintaining an ADL of around 5 across all membranes. Conductivity for all membranes increased with rising temperature (Fig. 6b). Generally, membranes with greater PA absorption yield higher conductivity due to the formation of a more complete hydrogen bonding network by the PA molecules. However, under the same doping amount, PBI-DA exhibits higher conductivity. Notably, as the temperature rises, PBI-DA shows a more pronounced growth rate in conductivity compared to the other two samples, this is likely due to the partial dissociation of DA bonds at elevated temperatures, resulting in a reduction in the polymer membrane's molecular weight resulting in a decrease in the molecular weight of the polymer membrane and an increase in the mobility of polymer segments, which may create more favorable pathways for proton transport and enhances proton conductivity. Beyond 170 °C, the high temperature and plasticizing effect of phosphoric acid caused the melting and fracture of the prepolymer PBI furan, preventing further testing, highlighting that higher molecular weight is a significant factor for the practical application of PBI. Furthermore, the membrane's conductivity conforms to Arrhenius behaviour, as illustrated in Fig. 6c. The corresponding activation energy was derived from linear fitting, revealing that the overall trend indicates an increase in activation energy with a decrease in PA content in membrane. Additionally, the activation energy of the chain-extended membrane is lower than that of the phenyl *m*-PBI of the same molecular weight, making it a more suitable material for PEM applications.

We soaked the polymer membrane in a 6 mol L^{-1} KOH solution for 14 days (Fig. 6d).[47,48] After the doping level remained stable, the samples were taken out for impedance testing. During the testing process, deionized water was added to the testing chamber and the anionic conductivity of the PBI membrane was tested at 100% relative humidity (Fig. 6e). When the temperature is below 50 °C, *m*-PBI with the highest alkali doping shows the highest anion conductivity. When the temperature rises above 50 °C, the conductivity growth rate of *m*-PBI decreases, while the conductivity of PBI-DA gradually increases and exceeds *m*-PBI. This may be due to the increase in temperature promoting the activity of water molecules in the membrane, allowing water molecules to enter the membrane and improve the transport efficiency of hydroxide

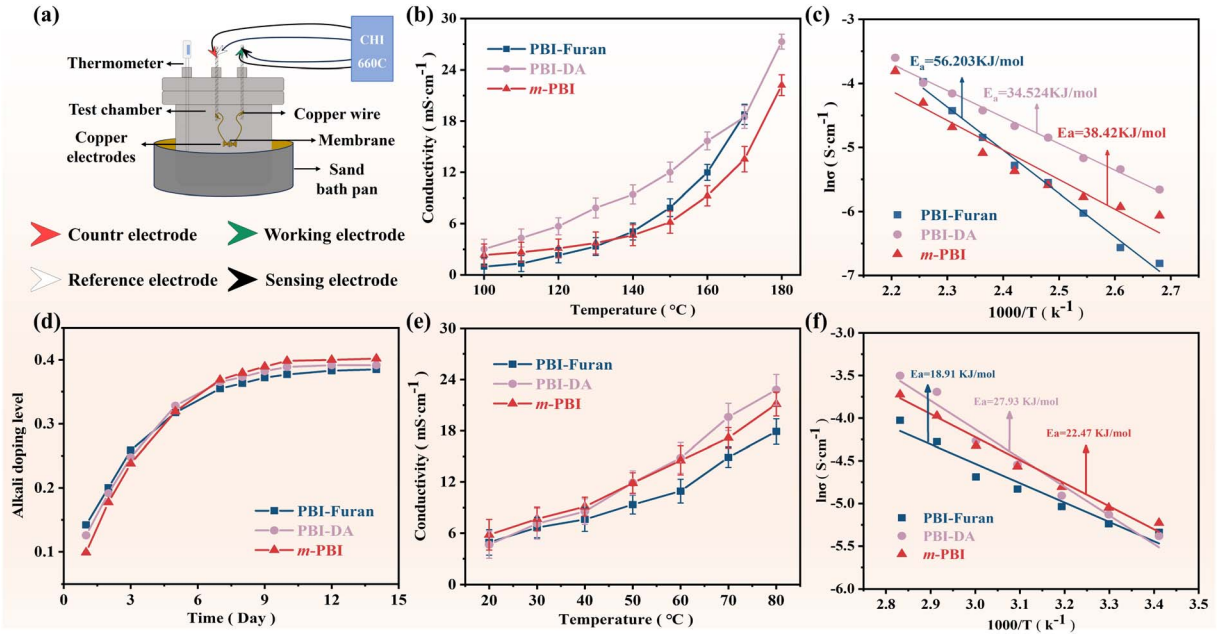

Fig. 6 (a) Simplified schematic diagram of testing device. (b) Proton conductivity of membranes as a function of temperature and (c) arrhenius plots of the proton conductivity of the PA-doped membranes for the calculation of activation energy (E_a) values. (d) Alkali doping level of polymer membranes after soaking in 6 M KOH for 14 days. (e) Anionic conductivity of membranes as a function of temperature and (f) arrhenius plots of the anionic conductivity of the OH^- doped membranes for the calculation of activation energy (E_a) values at 100%.

ions.[48] However, the dense membrane structure of *m*-PBI hinders the entry of most water molecules, resulting in a decrease in conductivity growth rate. In PBI-DA, the introduction of covalent bonds does not maintain a static state, and the DA covalent bonds increase the space between molecular chains, allowing part of water molecules to enter, resulting in an increase in water content in the membrane and a significant increase in conductivity. Similarly, the conductivity of the membrane also follows Arrhenius behaviour, as shown in Fig. 6f.

3.9 Self-healing and recycling performance

During the assessment of proton conductivity, we noted that the membrane exhibited melting behaviour at elevated temperatures, followed by re-solidification upon cooling, demonstrating reversible properties, which were not observed in *m*-PBI (Fig. 7a). To further explore the reversible characteristics of the membranes, we performed mechanical performance evaluations (Fig. 7b). The tensile strength recovery percentages for PBI-DA over three stretching cycles were recorded at 91.32%, 88.89% and 88.17% (Fig. 7c), demonstrating its capability to retain substantial strength even after multiple recycling iterations. Conversely, the recovery percentages for elongation at break were 60.50%, 52.54% and 45.12%, revealing a notable decline. We attribute this reduction in elongation at break to the incomplete resetting of dynamic covalent bonds during the recovery phase or insufficient recovery of the fracture contact surfaces. Nevertheless, the sample was able to maintain most of its mechanical properties, affirming its reversible characteristics and good recyclability.

To further substantiate the success of the DA and retro-DA reaction, we conducted temperature dependent FT-IR and DSC analyses on phosphate-doped PBI-DA membrane. Fig. 7d illustrates the temperature dependent FT-IR spectrum of PBI-DA. After phosphoric acid doping, the broad characteristic peaks observed in the 2500–3000 cm^{-1} range confirm the presence of phosphorylated polybenzimidazole. In addition, the characteristic peaks of HPO_4^{2-} and $H_2PO_4^-$ groups were detected at 1129.76 cm^{-1} and 955.63 cm^{-1}, respectively, indicating successful phosphorylation of PBI-DA. As the temperature rises, the hydrogen bond between phosphate groups and imidazole ring is disrupted, leading to deprotonation and contraction of the O–H and N–H cleavage widths. The infrared characteristic peak corresponding to HPO_4^{2-} and $H_2PO_4^-$ groups diminish and shift towards lower wavenumbers. When the temperature exceeds 90 °C, a decrease in the absorption intensity of the infrared peaks associated with C–N–C (from maleimide, 1393.46 cm^{-1}) and C–O–C (from furan, 1060.12 cm^{-1}) becomes evident, accompanied by a narrowing of the peak bands, signaling the onset of the retro-DA reaction.

Fig. 7e presents the DSC curve of PBI-DA membrane, revealing both an exothermic and an endothermic peak during the heating cycle. The pronounced exothermic peak at 71.78 °C is attributed to the exothermic DA reaction between the furan moiety from PBI-furan and bismaleimide, marking the optimal temperature for the DA reaction. A distinct endothermic peak was noted at 131.12 °C, which corresponds precisely to the reverse DA process of the dynamic covalent bonds. Collectively, the aforementioned data confirms that PBI-DA exhibits thermal reversibility and self-healing capabilities.

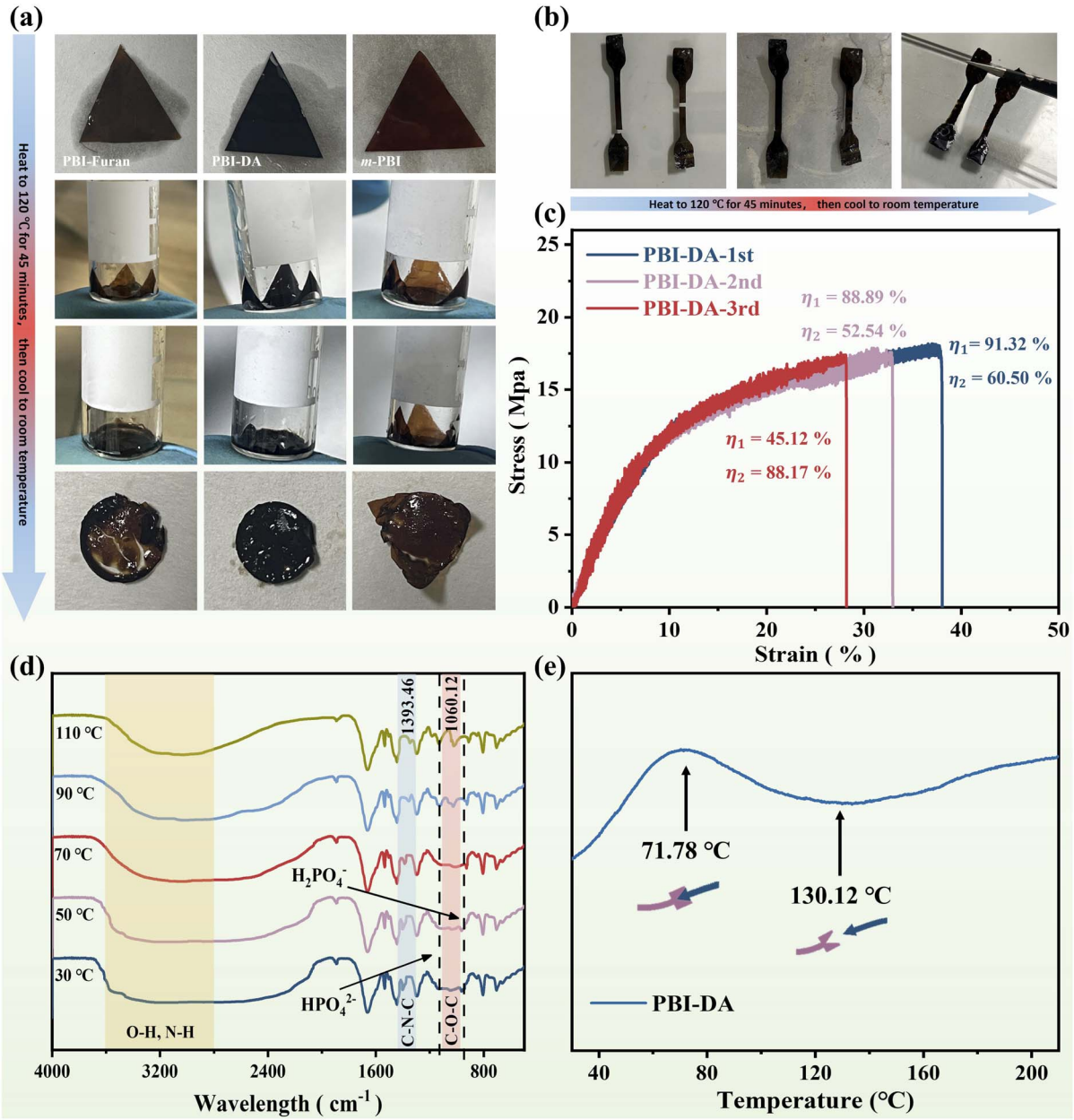

Fig. 7 (a) Melting behavior of phosphoric acid doped membranes at high temperature. (b) Self-healing behavior of PBI-DA spline at 120 °C. (c) Mechanical strength of self-healed PBI-DA spline. (d) The temperature dependent FT-IR spectrum of phosphoric acid doped PBI-DA membrane. (e) The DSC curve of PBI-DA membrane.

4 Conclusions

This study successfully designed and prepared PBI-DA based on Diels–Alder reaction chain extension using dynamic covalent chemistry strategy, and systematically investigated its synthesis process, dynamic mechanism, and physicochemical properties. In response to the problems of low solubility, insufficient mechanical strength, and non-recyclability of traditional PBI materials, DA reaction was innovatively introduced into PBI molecular design to construct a dynamically reversible linear PBI. The experimental results show that PBI-DA membrane exhibits excellent thermal stability (initial decomposition temperature >400 °C) and mechanical properties (tensile strength above 80 MPa), while the introduction of dynamic bonds endows the material with excellent abilities of self-healing at high temperature and recyclability. In terms of proton conductivity, PBI-DA membrane exhibits a proton conductivity of 15 mS cm^{-1} at 160 °C, and the swelling rate after phosphoric acid doping is less than 10%, meeting the long-term operation requirements of high-temperature fuel cells. However, it should be noted that the thermal reversibility of DA bonds may lead to high-temperature relaxation, and further optimization of dynamic bond density is needed to balance stability and reversibility. This study not only provides new

ideas for the green modification of PBI materials, but also promotes the development towards high-performance and sustainable fuel cell membrane materials through the design of dynamic covalent networks, laying an important foundation for the development of energy devices that combine efficient energy conversion and circular economy characteristics.

Author contributions

Hongting Pu planned and designed the project. Minjun Yin conducted all of the experiments. Minjun Yin and Hongting Pu analyzed the data and wrote the paper. All authors reviewed the manuscript.

Conflicts of interest

There are no conflicts to declare.

Data availability

The data supporting this study's findings are included within the article and its SI. Supplementary information is available: characteristic viscosity curve, part of mechanical properties and specific testing methods for conductivity are included here. See DOI: **https://doi.org/10.1039/d5ra05834a**.

Acknowledgements

This work is supported by the Major Program for Fundamental Research of Shanghai Science & Technology Commission, China (14JC1492700) and National Natural Science Foundation of China (52573344).

References

1 B. K. Clark and I. M. Robinson, *USP*, 1959, **2895**, 948.
2 K. Y. Wang, M. Weber and T. S. Chun, *J. Mater. Chem. A*, 2022, **10**, 8687–8718.
3 L. Hu, V. T. Bui, S. Fan, W. Guo, S. Pal, Y. Ding and H. Lin, *J. Mater. Chem. A*, 2022, **10**, 10872–10879.
4 J. H. Bitter and A. Asadi Tashvigh, *Ind. Eng. Chem. Res.*, 2022, **61**, 6125–6134.
5 J. Hu, R. Hardian, M. Gede, T. Holtzl and G. Szekely, *J. Membr. Sci.*, 2022, **648**, 120383.
6 J. Fang, X. Lin, D. Cai, N. He and J. Zhao, *J. Membr. Sci.*, 2016, **502**, 29–36.
7 R. Haider, Y. Wen, Z. F. Ma, D. P. Wilkinson, L. Zhang, X. Yuan, S. Song and J. Zhang, *Chem. Soc. Rev.*, 2021, **50**, 1138–1187.
8 H. T. Pu and Q. Z. Liu, *Polym. Int.*, 2004, **53**, 1512–1516.
9 H. T. Pu, L. D. Lou, Y. S. Guan and Z. H. Chang, *J. Membr. Sci.*, 2012, **415**, 496–503.
10 J. Li, W. Zhang, W. Wang, J. Ji, H. Li, Y. Sun, K. Li, T. Yang, W. Jin, Y. Tang, Y. Zhao, W. Li and C. Gong, *J. Mater. Chem. A*, 2024, **12**, 29054–29071.
11 K. Mochizuki, H. Iwatsu, M. Sudoh, M. Sudoh, Y. Ishiguro and T. Suzuki, *Electrochem. Commun.*, 2010, **78**, 129–131.
12 Z. H. Zou, M. J. Yin, P. Yin, Z. Hu, D. Wang and H. T. Pu, *Nano Energy*, 2024, **127**, 109774.
13 K. Friedrich, *Adv. Ind. Eng. Polym. Res.*, 2018, **1**, 3–39.
14 R. Peach, H. M. Krieg, A. J. Krüger, D. Bessarabov and J. Kerres, *Int. J. Hydrogen Energ.*, 2020, **45**, 2447–2459.
15 Y. Han, Y. Xu, K. Huang, F. Xu, J. Ji and B. Lin, *Int. J. Hydrogen Energ.*, 2024, **65**, 319–325.
16 M. Ueda, M. Sato and A. Mochizuki, *Macromolecules*, 1985, **18**, 2723–2726.
17 H. Zhong, Z. Fu, J. M. Taylor, G. Xu and R. Wang, *Adv. Funct. Mater.*, 2017, **27**, 1701465.
18 D. B. Shinde, H. B. Aiyappa, M. Bhadra, B. P. Biswal, P. Wadge, S. Kandambeth, B. Garai, T. Kundu, S. Kurungot and R. Banerjee, *J. Mater. Chem. A*, 2016, **4**, 2682–2690.
19 S. Chandra, T. Kundu, S. Kandambeth, R. BabaRao, Y. Marathe, S. M. Kunjir and R. Banerjee, *J. Am. Chem. Soc.*, 2014, **136**, 6570–6573.
20 H. Li, X. Ren, J. Dong, X. Che, R. Liu and J. Yang, *J. Electrochem. Soc.*, 2019, **166**, F1134.
21 N. J. Robertson, H. A. Kostalik IV, T. J. Clark, P. F. Mutolo, H. D. Abruña and G. W. Coates, *J. Am. Chem. Soc.*, 2010, **132**, 3400–3404.
22 J. Pan, Y. Li, L. Zhuang and J. Lu, *Chem. Commun.*, 2010, **46**, 8597–8599.
23 H. Wu, W. Wang, J. Ji, H. Li, J. Li, W. Zhang, K. Li, Q. Pei, X. Zhang, S. Zhang, W. Li and C. Gong, *J. Power Sources*, 2023, **567**, 232972.
24 Y. S. Oh, H. J. Lee, M. Yoo, H. J. Han and T. H. Kim, *J. Membr. Sci.*, 2008, **323**, 309–315.
25 T. Zhu, D. Zhu, J. Liang, L. Zhang, F. Huang and L. Xue, *J. Energy Chem.*, 2023, **85**, 91–101.
26 M. H. D. A. Farahani and T. S. Chung, *Sep. Purif. Technol.*, 2019, **209**, 182–192.
27 H. Y. Li and Y. L. Liu, *J. Mater. Chem. A*, 2013, **1**, 1171–1178.
28 P. Reutenauer, P. J. Boul and J. M. Lehn, *Eur. J. Org Chem.*, 2009, 1691–1697.
29 B. Masci, S. Pasquale and P. Thuéry, *Org. Lett.*, 2008, **10**, 4835–4838.
30 R. C. Boutelle and B. H. Northrop, *J. Org. Chem.*, 2011, **76**, 7994–8002.
31 C. D. Gutsche, D. E. Johnston and D. R. Stewart, *J. Org. Chem.*, 1999, **64**, 3747–3750.
32 L. R. Domingo and J. A. Sáez, *Org. Biomol. Chem.*, 2009, **7**, 3576–3583.
33 U. Pindur, G. Lutz and C. Otto, *Chem. Rev.*, 1993, **93**, 741–761.
34 S. Yang, X. Du, S. Deng, J. Qiu, Z. Du, X. Cheng and H. Wang, *Chem. Eng. J.*, 2020, **398**, 125654.
35 D. V. Zakharova, R. R. Aysin, A. A. Pavlov, D. A. Khanin, E. O. Platonova, Y. V. Nelyubina and A. V. Polezhaev, *Green Chem.*, 2025, **27**, 2263–2275.
36 O. A. O Alshammari, M. S. O Alhar, N. H. Elsayed, M. Monier and I. Youssef, *Int. J. Biol. Macromol.*, 2024, **275**, 133384.
37 N. N. Krishnan, N. M. H. Duong, A. Konovalova, J. H. Jang, H. S. Park, H. J. Kim, A. Roznowska, A. Michalak and D. Henkensmeier, *J. Membr. Sci.*, 2020, **614**, 118494.

38 A. A. A. Aljabali, A. Alkaraki, O. Gammoh, E. Qnais, A. Alqudah, V. Mishra and M. EI-Tanani, *RSC Adv.*, 2025, **15**, 27493–27523.
39 S. Pahari and S. Roy, *RSC Adv.*, 2016, **6**, 8211–8221.
40 S. Authayanun, K. Im-Orb and A. Arpornwichanop, *Chin. J. Catal.*, 2015, **36**, 473–483.
41 G. Skorikova, D. Rauber, D. Aili, S. Martin, Q. Li, D. Henkensmeier and R. Hempelmann, *J. Membr. Sci.*, 2020, **608**, 118188.
42 S. Wang, C. Zhao, W. Ma, N. Zhang, Z. Liu, G. Zhang and H. Na, *J. Power Sources*, 2013, **243**, 102–109.
43 J. S. Yang, Y. X. Xu, P. P. Liu, L. P. Gao, Q. T. Che and R. H. He, *Electrochim. Acta*, 2015, **160**, 281–287.
44 N. Zhang, C. J. Zhao, W. J. Ma, S. Wang, B. L. Wang, G. Zhang, Q. F. Li and H. Na, *Polym. Chem.*, 2014, **5**, 4939.
45 Z. H. Chang, H. T. Pu, D. Wan, M. Jin and H. Pan, *Polym. Degrad. Stab.*, 2010, **95**, 2648–2653.
46 P. J. Zhang, B. Shen and H. T. Pu, *Polymer*, 2022, **245**, 124698.
47 V. Sinigersky, D. Budurova, H. Penchev, F. Ublekov and I. Radev, *J. Appl. Polym. Sci.*, 2013, **129**, 1223–1231.
48 Q. X. Wu, Z. F. Pan and L. An, *Renew. Sust. Energ. Rev.*, 2018, **89**, 168–183.